Volume 1 | Number 1 | Jan 2013 | Pages 1–100

Soft Matter

www.rsc.org/softmatter

Wrinkled stripes localized by cracks in metal films deposited on soft substrates†

Senjiang Yu,* Xiaofei Zhang, Xiaofei Xiao, Hong Zhou and Miaogen Chen

Department of Physics, China Jiliang University, Hangzhou 310018, PR China.

E-mail: sjyu@cjlu.edu.cn; senjiangyu@hotmail.com

† *Electronic supplementary information (ESI) available.*

Homogeneous global wrinkling patterns such as labyrinths, herringbones, ripples and straight stripes can be widely observed in natural and artificial systems, but localized wrinkling patterns (not including buckle-driven delaminations, folds, ridges and creases) are seldom observed in experiments. Here we report on the spontaneous formation of highly ordered wrinkled stripes localized by cracks in metal films deposited on soft substrates. The experiment shows that the metal film is under a large tensile stress during deposition, which is relieved by the formation of networked cracks. After deposition, a compressive stress is stored up in the film and it always focuses near the new formed cracks due to the plastic deformation of the film, resulting in the formation of localized wrinkled stripes composed of a large number of straight wrinkles perpendicular to the cracks. The morphological characteristic, formation mechanism and evolution behaviors of the localized wrinkled stripes have been described and discussed in detail.

Introduction

Fascinating structures and morphologies induced by residual stress or constrained growth can be widely observed in natural and artificial systems that span a wide range of scales, from macroscopic tectonic plates, ground surfaces, elastic sheets,[1,2] textile fabrics,[3] plant leaves, flowers, fruits,[4,5] human skins,[5,6] biological tissues[4,5] to nanometer-scaled films, coatings, graphenes[3,7] and nanotubes.[8] For film/substrate bilayers, which are now widely used in many high-tech applications, the stress relief mechanisms are closely related to the stress property (tensile or compressive) and the substrate elasticity. In the case of tensile stress, the film tends to form various fracture patterns such as networked, straight, sinusoidal, spiral and crescent cracks when the tensile stress is beyond the breaking strength of the film.[9,10] The substrate property and film thickness can determine the number, width and morphology of the cracks.[10,11] In the case of compressive stress, a variety of stress modes can be observed and they are strongly determined by the elasticity of the substrate. If the substrate is stiff, the film tends to partially delaminate from the substrate and form various localized delaminating patterns such as straight-sided, circular, varicose and telephone cord buckles.[12-15] If the substrate is elastic, the film tends to form homogeneous wrinkling patterns such as labyrinths, herringbones, ripples and straight stripes.[6,16-18] Meanwhile, the interfacial adhesion is strong and the film remains well attached to the substrate. As the interfacial adhesion decreases or the substrate rigidity increases, the wrinkling mode may change into the localized buckle-delamination mode.[19,20] If the substrate is very soft or liquid, the film tends to form homogeneous

sinusoidal wrinkles under modest compression. These sinusoidal wrinkles may turn

into localized folds or ridges with further increasing the compression.[21-23] Another

localized stress mode, namely crease, can be widely observed in pure soft matters

(without capped rigid layers) such as gel, hydrogel, biological tissues under the

compression or constrained growth.[24,25]

The homogeneous sinusoidal wrinkles possess a broad distribution of stress

energy, while the localized modes including the cracks, buckle-driven delaminations,

folds (or ridges) and creases can well focus the stress energy. Both the homogeneous

wrinkling patterns and localized stress modes have been extensively investigated in

the past decades. Controlled wrinkled surface is useful for a wide range of

applications including flexible electronics,[26,27] tunable optical grating,[28] microfluidic

channel,[29] marine antifouling,[30] smart adhesion,[31,32] hydrophobicity,[33] measurement

technique[34,35] and self-assembly ordered microstructures.[36] To use the wrinkling

patterns as functional devices, it is intrinsic and necessary to precisely control the

formation and geometry of the wrinkles. Extensive studies have explored possible

ways to manipulate the compression in the film and thus to generate the controlled

wrinkled surface.[17] It is well known that uniaxial compression in the film induces

straight wrinkles while equi-biaxial compression usually induces labyrinth or

herringbone patterns. The ordered wrinkling morphologies can be well tuned by

locally altering the equi-biaxial stress state in the film. Effective tuning techniques

include uniaxial loading/unloading,[28,34,35] progressively released biaxial strain,[37]

lithographically prepatterned substrate,[38] selective interfacial adhesion,[39] spatially

sequential wrinkling,[40] contact-line mechanics,[41] mechanically-induced surface

defect,[42] constrained edge effect,[3,43] etc.

Although the localized stress modes such as cracking, delaminating, folding and

creasing are very common in natural and artificial systems, the localized wrinkling

patterns are seldom observed in experiments. In this paper, we report on the

spontaneous formation of highly ordered wrinkled stripes localized by cracks in metal

films deposited on soft substrates. The brittle metal film spontaneously fractures to

form networked cracks under the tensile stress during deposition. After deposition, the

compressive stress induced by the thermal contraction of the soft substrate always

focuses near the new formed cracks. The stress component perpendicular to the crack

can be released by sliding of the film pieces, while the stress component parallel to

the crack is relieved by formation of high ordered wrinkled stripe composed of a large

number of straight wrinkles perpendicular to the crack. Our experimental technique

can be developed to effectively maneuver the dimension and orientation of the

localized wrinkles by introducing regularly arranged surface defects (such as cracks)

into the film before the wrinkles form. Highly ordered wrinkling patterns may be

beneficial for a wide range of technological applications.

Results and discussion

Morphologies of the cracks and wrinkles

The typical surface morphologies of metal films (here is iron) deposited on PDMS

substrates under different deposition times (i.e., with varied film thicknesses) are

shown in Fig. 1. We find that if the film thickness is very small (h < 30 nm), the film is homogenous and rough under the optical microscopy (see Fig. 1a). In order to detect more structural details of the rough surface, atomic force microscopy (AFM) images have been taken and the typical results are shown in Fig. 2. It is clear that only disordered wrinkles (labyrinths) form in the film with small thickness because of an isotropic stress field. The wrinkle wavelength increases obviously with increasing the film thickness, in good agreement with many previous experimental observations.[34,35,44]

When the film thickness is larger than a certain value (about 30 nm), cracks start to form in the film and the whole film surface is divided into several closed domains. At the same time, the homogeneous disordered wrinkles degenerate quickly and finally disappear completely, as shown in Fig. 1b. The crack number increases obviously with increasing the film thickness and thus the sizes of the closed domains decrease greatly. The evolution of the domain width (i.e., the spacing between neighboring cracks) d with the film thickness h is shown in Fig. 3c. It is clear that as the film thickness increases, the domain width decreases drastically first, and then it reaches a stable value. The experimental data can be well fitted by an exponential decay equation, i.e., $d = d_{sat} + d_{decay}e^{-(h-h_0)/H}$, where d_{sat} represents the saturation domain width, d_{decay} represents the decay value, h_0 represents the critical point that the cracks start to appear ($h_0 \approx$ 30 nm in this case), H is a constant, representing the decay rate of the domain width with film thickness. In Fig. 3c, the saturation domain width is about 158.8 µm and the constant H is about 15.5 nm.

Fig. 3a shows the enlarged morphologies of the cracks in the film with $h = 90$ nm.

An unexpected result is that two types of crack morphologies can be seen clearly. One

is gray under the optical microscopy (namely old crack, which is formed earlier and is

covered with a thin layer of film later, for details see the following description), while

the other is very dark and is accompanied by a wrinkled stripe (namely new crack,

which is almost not covered by the subsequent deposited film). The wrinkled stripe is

composed of a large number of parallel straight wrinkles, which are perpendicular to

the crack. In general, the stripe width (i.e., the length of the straight wrinkles) L is

uniform for each wrinkled stripe. When the old crack and new crack cross with each

other, their morphologies are almost unchanged although the straight wrinkles at the

intersection are somewhat distorted (see Fig. 3a). The dependences of the widths of

the old and new cracks on the film thickness are shown in Fig. 3d. We find that the

old crack width is almost unchanged and the average value is about 2 μm. On the

other hand, the new crack width increases steadily with increasing the film thickness.

Fig. 3b shows the 3-D structural information of the new crack and wrinkled

stripe. The 2-D AFM images and corresponding profiles of the old and new cracks

can refer to the ESI† (Fig. S1). We find that the height along the ridge of the straight

wrinkle is almost uniform except for the crack edges, where two peaks can be

observed.[45] When approaching to the wrinkle boundary, the height decreases quickly

to a plateau representing the flat film surface. The film remains well attached to the

PDMS foundation and no obvious delamination is detected. According to the

theoretical prediction,[19,20] the wrinkling-induced delamination can occur when the

compression is large or the interface bonding is weak. Although the highly hydrophobic PDMS tends to not stick to metals in many cases (evaporating deposited films,[38,46] for example), the interfacial adhesion can be improved greatly due to the radiation from plasma and the bombardment from high energy particles by using sputtering technique. Thus, the wrinkling-induced delamination is suppressed.

Our experiment also shows that when the film thickness increases, the crack morphologies become more complex. An example of the crack morphologies in the film with $h = 225$ nm is shown in Fig. 4. The 2-D AFM images and corresponding profiles of the cracks can refer to the ESI† (Fig. S2). It is shown that three types of cracks can be seen clearly: the old crack (mode I), the mixed crack morphology without accompanied wrinkled stripe (mode II) and the new crack or mixed crack with localized winkled stripe (mode III). Due to the elastic deformation of the soft substrate, each crack edge exhibits a peak.[45]

Formation mechanisms of the cracks and wrinkles

Cracking and wrinkling patterns can be widely observed in nature and experiments, especially in film/substrate bilayers under residual stresses. It is well known that the cracks are generated under the residual tensile stress while the wrinkles form under the residual compressive stress. The residual stresses can be generated by many factors such as the deposition process, lattice mismatch between the substrate and the film, thermal expansion mismatch,[38] solvent diffusion into the film,[14,47] bubble inflation in the film,[48] hydrogen absorption,[13] capillarity,[49] external

loading,[28,34,35,37] etc. We suggest that the networked cracks and localized wrinkles appeared in our experiment are induced by the tensile stress stored up during deposition and the compressive stress generated after deposition, respectively. The tensile stress and compressive stress are both due to the thermal expansion mismatch between the PDMS substrate and the metal film when the temperature changes.

According to many previous studies,[38,43] the temperature of the soft elastic substrate would increase obviously during deposition owing to the heat radiation from the target and the bombardment from the high energy particles. As a result, the PDMS substrate thermally expands and places the film under a tensile stress. This tensile stress increases approximately linearly with the deposition time. When the tensile stress is beyond the breaking strength of the metal film, cracks start to form in the film. As shown in Fig. 3d, the old crack width is almost unchanged with increasing the film thickness, implying that once the local tensile stress reaches the critical value, the crack expands to a certain width instantaneously. After that, the local tensile stress is released and the crack expansion is stopped. Then the deposited atoms will land on the film surface and the crack region simultaneously, which results in the formation of a new film inside the crack. The new formed film is thinner than other film regions (see the inset of Fig. S2d) and it can be detected by the optical microscopy and AFM clearly. Since a new film has formed in the crack region, such crack is called as old crack.

When the film deposition continues, the tensile stress increases gradually and reaches a critical value again, which results in the formation of a new crack. It seems

that as the film thickness increases, the breaking strength of the iron film increases accordingly. It needs a larger tensile stress to break the film and thus the width of the new crack increases with increasing the film thickness, as shown in Fig. 3d. Our experiment also shows that if the film thickness is small, the new formed crack tends to appear in the continuous film region since the closed domain is quite large in this case. When the film thickness increases, the closed domain size decreases greatly. Then the new formed crack tends to extend along the old crack edge and thus the mixed crack morphology forms (see Figs. 4 and S2). Because the new formed crack tends to extend along the old crack edge, the domain size is almost unchanged with further increasing the film thickness, as shown in Fig. 3c.

After deposition, when the sample cools to the ambient temperature, the PDMS substrate thermally contracts and places the metal film under a compressive stress. If the film thickness is very small ($h < 30$ nm), no crack forms in the film and therefore the compressive stress is relieved by the formation of disordered homogeneous wrinkles due to the isotropic stress field, as shown in Fig. 2. When the film thickness increases, a large number of broad cracks form during deposition. These cracks can effectively release the thermal compression of the film and thus the global homogeneous wrinkles disappear. At the same time, the film near the new crack undergoes a strong plastic deformation. The compressive stress can focus in the plastic deformation zone and thus the wrinkled stripe is localized in the vicinity of the new crack. As the deposition continues, a new film forms inside the crack and the strong plastic deformation will disappear gradually. Therefore, the localized wrinkles

can not be observed near the old crack. The detailed theoretical analysis for the formation and evolution of the plastic deformation and wrinkling pattern near the crack will be published elsewhere.

The compressive stress localized by the new crack should be biaxial. We suggest that the stress component parallel to the crack is relieved by the formation of straight wrinkles perpendicular to the crack. The stress component perpendicular to the crack can be released by sliding of the film pieces, resulting in the decrease in the crack width. This can explain the experimental result that the new crack width is smaller than the average old crack width when the film thickness is very small, as shown in Fig. 3d. Because the plastic deformation zone near the new crack is symmetric, the half lengths of the straight wrinkles beside the two crack edges are always equal, as shown in Fig. 3. For the mixed crack mode, the old crack and the surrounding film region can be regarded as a cohesive whole and thus the half lengths of the straight wrinkles beside the two edges of the new crack are equal, as shown in Figs. 4 and S2.

Evolution of the wrinkled stripe with film thickness

Fig. 5 shows the 2-D AFM images and corresponding profiles of the localized wrinkled stripes with varied film thicknesses. The morphological evolution of the wrinkled stripes with the film thickness taken by the optical microscopy can refer to the ESI† (Fig. S3). It is clear that the parallel straight wrinkles are well periodic and their wavelength and amplitude both increase with the film thickness. The crack width increases obviously with increasing the film thickness, which is similar to the result

10

shown in Fig. 3d. Our experiment shows that the new cracks are always accompanied by the wrinkled stripes and the stripe widths in each sample are almost uniform. If the film thickness is much large, the wrinkled stripes may degenerate gradually and finally disappear completely. In order to further understand the evolution behaviors of the wrinkled stripe, we measured the dependences of the wrinkle length L, wavelength λ, amplitude A, their ratio A/λ on the film thickness h, and the results are shown in Fig. 6. We find that in the range of $h = 30$–200 nm, the wrinkle length is almost unchanged. When the film thickness is larger than 200 nm, however, the wrinkled stripe starts to degenerate and the wrinkle length decreases steadily. The wrinkle wavelength and amplitude have the same evolution trend: they increase linearly in the smaller film thickness range while deviate from linearity when $h > 300$ nm. The ratio of A/λ is almost unchanged with increasing the film thickness and the average value is about 0.087 (see Fig. 6d). The fact that the ratio A/λ is less than 0.1 means that such wrinkle is very shallow compared to high aspect ratio wrinkles (e.g., $A/\lambda > 0.5$),[50,51] creases,[24,25] folds[21,22] and ridges[23] in soft matters. The small value of A/λ also implies that the continuum elastic theory is valid in this case.

Many previous works utilized a simple stress model to explain the wrinkle behavior of a thin, stiff film resting on an infinite thick, soft elastic substrate. The analysis of energy minimization (including the stretching and bending energies of the film and the elastic energy of the substrate) shows that the equilibrium wrinkle wavelength λ, amplitude A and critical strain ε_c obey the following scaling laws

$$\lambda = 2\pi h[\frac{E_f(1-v_s^2)}{3E_s(1-v_f^2)}]^{1/3}, \tag{1}$$

11

$$A = h(\frac{\varepsilon}{\varepsilon_c})^{\frac{1}{2}},$$ (2)

$$\varepsilon_c = \frac{1}{4}[\frac{3E_s(1-v_f^2)}{E_f(1-v_s^2)}]^{\frac{2}{3}}.$$ (3)

Here E is the elastic modulus, v is the Poisson's ratio, h is the film thickness, ε is

the residual strain, the subscripts f and s refer to the film and substrate respectively.

Given the mechanical properties of the film and substrate are both constant, the

wrinkle wavelength is proportional to the film thickness, which can well explain the

experimental results when the film thickness is less than 300 nm. As $h > 300$ nm,

however, the wrinkle wavelength is much lower than the theoretical predication,

meaning that the assumption of infinite thick substrate is invalid. In our experiment,

the thickness of PDMS substrate is about 15 μm. When the film thickness reaches

several hundreds nanometers, the effect of substrate thickness can not be neglected.

Recently, the influence of the substrate thickness on the wrinkle wavelength has been

analyzed and the wavelength can be given by[36,52]

$$\frac{\lambda}{2\pi h_f} = [\frac{Y}{1+\sqrt{1+12Y(\frac{h_f}{h_s})^3}}]^{\frac{1}{3}},$$ (4)

where $Y = \frac{1}{2(1-v_f^2)} \times \frac{E_f}{E_s}$. Assuming that the elastic modulus of the metal film is 200

GPa, the Poisson's ratio is 0.3 and the elastic modulus of PDMS is 2 MPa. Then the

parameter Y can be estimated to be about 5×10^4. For the largest film thickness in

our experiment ($h_f = 450$ nm), the ratio h_s/h_f is about 33 and thus $\frac{\lambda}{2\pi h_f} \approx 21.3$. This

value is much smaller than the corresponding value obtained from eq (1)

$(\dfrac{\lambda}{2\pi h_{\mathrm{f}}} \approx 32.2\,)$, in good agreement to the experimental result shown in Fig. 6b.

According to eqn (1)-(3), the wrinkle amplitude can be expressed as $A \propto \lambda\sqrt{\varepsilon}$. Based on the fact that the total compressive stress energy and crack number both increase with the film thickness, we suggest that the local compressive stress near the new crack is almost unchanged. Therefore, the wrinkle amplitude is only dependent on the wrinkle wavelength. They have the same evolution trend: increasing linearly in the smaller film thickness range but deviating from linearity when $h > 300$ nm due to the effect of finite thick substrate. Since the local compressive stress near the new crack is uniform, the ratio A/λ is almost unchanged with increasing the film thickness, as shown in Fig. 6d. On the other hand, the theoretical analysis shows that the plastic deformation zone near the crack first increases and then decreases with increasing the film thickness. Thus the localized wrinkles degenerate gradually in the larger film thickness range.

Evolution of the wrinkled stripe with substrate property

According to the analysis above, the wrinkle wavelength not only depends on the film thickness, but also relates to the substrate property (mainly the elastic modulus). Here we shall investigate the effect of the PDMS property on the localized wrinkles. It is well known that the as-prepared PDMS is colloidal state and it needs to be cured at a higher temperature (e.g., 80°C) for a certain period to form completely crosslinked elastic foundation.[53-55] Therefore, we changed the curing time of the PDMS gel from 0 to 4 hours when the curing temperature was fixed at 80°C. Then the PDMS

13

substrates cured with different times were placed into the sputtering chamber for film deposition immediately. The typical surface morphologies of the iron films deposited on the PDMS substrates with varied curing times are shown in Fig. 7a. The old crack and new crack can be seen clearly for all the samples and no homogeneous disordered wrinkle forms in the film. As the curing time T_c increases, the crack number increases obviously.

Fig. 7b shows the morphological evolution of the wrinkled stripe with the curing time taken by AFM. The optical micrographs can refer to the ESI† (Fig. S4). Fig. 7c shows the corresponding profiles of the straight wrinkles with varied curing times. It is clear that the parallel straight wrinkles are well periodic and their wavelength and amplitude both decrease with increasing the curing time. When the curing time increases, the crack width and wrinkle length both decreases obviously. In order to further understand the evolution behaviors of the wrinkled stripe, we measured the dependences of the crack spacing (i.e., the domain width) d, crack width w, wrinkle length L, wavelength λ, amplitude A, their ratio A/λ on the curing time T_c, and the results are shown in Fig. 8. We find that the domain width, crack width, wrinkle length, wavelength and amplitude all have the same evolution trend. When the curing time increases, these parameters decrease drastically first, and then the decay speeds slow down and finally they approach to respective stable values. All the experimental data can be well fitted by the same exponential decay equation (see Fig. 8). For example, the wrinkle length can be fitted by $L = L_{sat} + L_{decay}e^{-T_c/T_{c0}}$, where L_{sat} represents the saturation wrinkle length, L_{decay} represents the decay value and T_{c0} is

a time constant, representing the decay rate of the wrinkle length with curing time. In

Fig. 8, the saturation values of the domain width, new crack width, wrinkle length,

wavelength and amplitude are about 201, 4.7, 31.4, 6.2 and 0.49, respectively. The

transition time points for these parameters are all about $T_c = 5$ min. When $T_c > 5$ min,

these parameters are almost unchanged with increasing the curing time. Interestingly,

the ratio A/λ exhibits two levels divided by $T_c \approx 5$ min. When $T_c < 5$ min, all the

experimental data are above 0.09 (about 0.095). When $T_c > 5$ min, however, the

experimental data drop down to about 0.082.

The experiment shows that the uncured PDMS is colloidal state. As the curing

time increases, the liquid PDMS crosslinks and turns into elastic material gradually.

Therefore, the equivalent elastic modulus of the PDMS substrate and the interfacial

adhesion between the PDMS and the metal film may increase greatly with increasing

the curing time.[53-55] Many previous studies showed that the crack number and

morphology are strongly dependent on the interfacial adhesion between the film and

the substrate. If the interfacial adhesion is weak, the tensile stress tends to be released

by the sliding of the broken film pieces.[11] If the interfacial adhesion is strong,

however, the tensile stress tends to be released by the formation of new intersectional

cracks.[10] Therefore, sparse but broad cracks are favorable for weak adhesion cases

(e.g., the tectonic plates in geography or thin films floating on a liquid surface), while

a dense crack network is favorable for strong adhesion cases (e.g., the ceramic paints,

dried mud or thin films deposited on a solid substrate).

In our experiment, we suggest that the tensile stress stored up during deposition

and the compressive stress generated after deposition are both uniform for different curing times since the deposition time (film thickness) is fixed. If $T_c = 0$, the PDMS foundation is colloidal state and the interfacial adhesion is very weak. Therefore, the crack number is very small but the width is very large. When the curing time increases, the interfacial adhesion energy increases gradually and thus the crack number increases but the width decreases. On the other hand, the equivalent elastic modulus of the PDMS increases with increasing the curing time. According to eqn (1)-(3), when the elastic modulus of the substrate increases, the wrinkle wavelength and amplitude both decrease, as shown in Figs. 8d and e. When $T_c > 5$ min, the PDMS has been crosslinked completely and then the interfacial adhesion energy and the elastic modulus of the substrate are almost unchanged. Therefore, the crack number, crack width, wrinkle wavelength and amplitude are all constants when $T_c > 5$ min.

Furthermore, the appearance of two levels of A/λ divided by $T_c \approx 5$ min should be attributed to the change of the substrate property. We believe that the uncured or partially cured PDMS substrates exhibit viscoelastic behaviors and they are comparatively soft. Therefore, the ratio A/λ is somewhat larger compared to the completely elastic substrates when $T_c > 5$ min (see Fig. 8f). Unfortunately, uncertainty with respect to the structure and property of the PDMS with different curing times makes it difficult to provide a more quantitative discussion. This will be addressed properly in the future. Although the ratio A/λ exhibits two levels for different PDMS substrates, we also notice that the difference of A/λ is not very large (about 0.095 for $T_c < 5$ min and 0.082 for $T_c > 5$ min). According to eqn (1)-(3), the ratio

A/λ is proportional to $\sqrt{\varepsilon}$. The residual strain ε for $T_c > 5$ min roughly equals to

75% of the strain for $T_c < 5$ min. Therefore, the stress energy density stored in the

wrinkled area is almost uniform for different curing times.

Finally we shall discuss the underlying mechanism for selecting and determining

the width of the wrinkled stripe. We notice that the wrinkled stripe width L and the

closed domain width d have the same evolution trend with increasing the curing time

(see Figs. 8a and c). Their ratio L/d, representing relative wrinkled area, should be

related to the residual compressive stress. Since the total compressive stress of the

film is uniform for different curing times when the film thickness is fixed, the relative

wrinkled area is almost unchanged with increasing the curing time, as shown in the

inset of Fig. 8c. The obvious reduction of L/d for $T_c < 1$ min should be attributed to

the weak interfacial adhesion and larger stress energy density. It can be concluded

here that the wrinkled stripe width is dependent on the combination of the stress value

and the wrinkled stripe number. One then can effectively maneuver the width and

orientation of the localized wrinkles by introducing regularly arranged surface defects

(such as cracks) into the film before the wrinkles form. The wavelength and amplitude

of the wrinkles can be controlled by altering the film thickness and substrate elasticity.

The highly ordered wrinkles may be used in a wide range of applications such as

smart adhesion, friction, liquid flow, wettability, reflectivity, cell growth, stamping,

sensing, coating and measuring etc. However, it should be noted here that the length

scale limitation of the localized wrinkles may be a fatal weakness for many possible

applications. To generate large-scaled parallel wrinkles in a sample, further

17

experimental and theoretical studies are needed, including designing the crack array, controlling the crack density, improving the interfacial adhesion and tuning the compressive stress.

Conclusions

In summary, highly ordered wrinkled stripes localized by cracks in metal films deposited on soft PDMS substrates are described and discussed in detail. The morphologies of the cracks and wrinkles are closely related to the film thickness and substrate property. The networked cracks (including old crack, new crack and mixed crack) are resulted from the tensile stress stored up during deposition. The crack number and width both increase with increasing the film thickness owing to the increase in the total stress energy. As the curing time of the PDMS increases, the crack width decreases but the crack number increases. The localized wrinkled stripe, composed of a large number of straight wrinkles perpendicular to the crack, is induced by the compressive stress after deposition. The wrinkle wavelength and amplitude increase approximately linearly with the film thickness, but they both decreases with the curing time in compliance with a simple exponential law. The wrinkled strip width is proven to be determined by the combination of the compressive stress value and the crack number. One then can tune the wrinkled stripe width by controlling the crack number and the stress value. We anticipate that the experimental results presented in this paper will provide a deep insight into the localized wrinkling phenomena, which are greatly distinguished from the well known

localized stress patterns such as buckle-driven delaminations, folds, ridges and creases.

Furthermore, the controllable formation of highly ordered wrinkles may be beneficial

for the technological applications in optical devices, flexible electronics, fluid

handling systems, micro-electro-mechanical systems, biological templates etc.

Experimental

Substrate preparation

Completely or partially cross-linked polydimethylsiloxane (PDMS) (Dow Corning's

Sylgard 184) was used for the soft elastic substrates. The prepolymer and cross-linker

were mixed with 10:1 volume ratio. After degassing, the PDMS colloid was

spin-coated onto clean glass slides with the size of about 10×10 mm^2. The substrates

were then cured at 80 °C for different periods and then naturally cooled in air.

Generally, the curing time is larger than 3 hours to obtain the completely cross-linked

PDMS (pure elastic substrate). To investigate the influence of the substrate property

on the localized wrinkles, the curing time was changed from 0 to 4 hours when the

curing temperature was fixed at 80°C. Therefore, the partially cross-linked PDMS

was obtained ant its property was continuously changed with the curing time. Then

the uncured and partially cured PDMS substrates were placed into the sputtering

chamber for film deposition immediately because their properties can change slowly

in the ambient temperature. The natural curing process of the PDMS in the ambient

temperature was in the range of 2-3 days. The resulting PDMS substrates had the

thickness of about 15 μm (Fig. S5 of the ESI†).

Film fabrication

The films were prepared by direct current (DC) magnetron sputtering at room temperature. The target was a piece of iron disk (purity 99.9%) with a diameter of 60 mm and a thickness of 3 mm. It should be noted here that the film material is not restricted to iron. Similar localized wrinkles can be found in a variety of metals, including chromium, silver, cobalt etc. Furthermore, the substrate material is also not restricted to PDMS. Similar localized wrinkles can also form in silicone oil, silica gel and jelly glue foundations. The target-substrate distance was about 80 mm. The residual gas pressure before sputtering was below 2×10^{-4} Pa. The films were deposited under argon gas (purity 99.99%) in pressure of 0.5 Pa. The sputtering power was fixed to be 50 W. Under this sputtering power, the deposition rate of the film was about 0.25 nm/sec. After deposition, the film thickness was calibrated by a profilometry (α-step 200 profilometer, TENCOR). The samples with varied film thicknesses were obtained by changing the deposition time from 10 sec to 30 min, which was controlled precisely by a computer.

Characterization

The surface morphologies of the films were taken by an optical microscopy in reflected light mode (Leica DMLM), equipped with a charge-coupled device camera (Leica DC 300), which was interfaced to a computer for data storage and processing. The 3D information of the cracking and wrinkling patterns was determined by an

atomic force microscopy (AFM, Veeco Dimension 3100, Bruker) operated in tapping

mode. The collected data consisted of height information on square 256×256 arrays of

pixels with areas ranging from 5×5 to 85×85 μm^2.

Acknowledgements

References

1   E. Cerda and L. Mahadevan, *Phys. Rev. Lett.*, 2003, **90**, 074302.

2   A. Lucantonio, M. Roché, P. Nardinocchi and H. A. Stone, *Soft matter*, 2014, **10**,
    2800–2804.

3   H. Vandeparre, M. Piñeirua, F. Brau, B. Roman, J. Bico, C. Gay, W. Bao, C. N.
    Lau, P. M. Reis and P. Damman, *Phys. Rev. Lett.*, 2011, **106**, 224301.

4   B. Li, Y. P. Cao, X. Q. Feng and H. Gao, *Soft Matter*, 2012, **8**, 5728–5745.

5   X. Chen and J. Yin, *Soft Matter*, 2010, **6**, 5667–5680.

6   J. Genzer and J. Groenewold, *Soft Matter*, 2006, **2**, 310–323.

7   W. Bao, F. Miao, Z. Chen, H. Zhang, W. Jang, C. Dames and C. N. Lau, *Nat. Nanotech.*, 2009, **4**, 562–566.

8   S. B. Hutchens, L. J. Hall and J. R. Greer, *Adv. Funct. Mater.*, 2010, **20**, 2338–2346.

9   J. Marthelot, B. Roman, J. Bico, J. Teisseire, D. Dalmas and F. Melo, *Phys. Rev. Lett.*, 2014, **113**, 085502.

10   V. Lazarus and L. Pauchard, *Soft Matter*, 2011, **7**, 2552–2559.

11   P. G. Cai, S. J. Yu, X. J. Xu, M. G. Chen, C. H. Sui and G. X. Ye, *Appl. Surf. Sci.*, 2009, **255**, 8352–8358.

12   B. Audoly, *Phys. Rev. Lett.*, 1999, **83**, 4124–4127.

13   A. Pundt, E. Nikitin, P. Pekarski and R. Kirchheim, *Acta Mater.*, 2004, **52**, 1579–1587.

14   K. Lee, S. Lee, D. Y. Khang and T. Lee, *Soft Matter*, 2010, **6**, 3249–3256.

15   S. J. Yu, X. F. Xiao, M. G. Chen, H. Zhou, J. Chen, P. Z. Si and Z. W. Jiao, *Acta Mater.*, 2014, **64**, 41–53.

16   S. Cai, D. Breid, A. J. Crosby, Z. Suo and J. W. Hutchinson, *J. Mech. Phys. Solids*, 2011, **59**, 1094–1114.

17   S. Yang, K. Khare and P. C. Lin. *Adv. Funct. Mater.*, 2010, **20**, 2550–2564.

18   T. R. Hendricks, W. Wang and I. Lee, *Soft Matter*, 2010, **6**, 3701–3706.

19   H. Mei, R. Huang, J. Y. Chung, C. M. Stafford and H. H. Yu, *Appl. Phys. Lett.*,

2007, **90**, 151902.

20   K. Pan, Y. Ni, L. He and R. Huang, *Int. J. Solid Struct.*, 2014, **51**, 3715–3726.

21   L. Pocivavsek, R. Dellsy, A. Kern, S. Johnson, B. Lin, K. Y. C. Lee and E. Cerda, *Science*, 2008, **320**, 912–916.

22   P. Kim, M. Abkarian and H. A. Stone, *Nat. Mater.*, 2011, **10**, 952–957.

23   J. Zang, X. Zhao, Y. Cao and J. W. Hutchinson, *J. Mech. Phys. Solids*, 2012, **60**, 1265–1279.

24   S. Cai, D. Chen, Z. Suo and R. C. Hayward, *Soft Matter*, 2012, **8**, 1301–1304.

25   T. Tallinen, J. S. Biggins and L. Mahadevan, *Phys. Rev. Lett.*, 2013, **110**, 024302.

26   D. Y. Khang, J. A. Rogers and H. H. Lee, *Adv. Funct. Mater.*, 2009, **19**, 1526–1536.

27   J. A. Rogers, T. Someya and Y. Huang, *Science*, 2010, **327**, 1603–1607.

28   C. Yu, K. O'Brien, Y. H. Zhang, H. Yu and H. Jiang, *Appl. Phy. Lett.*, 2010, **96**, 041111.

29   T. Ohzono, H. Monobe, K. Shiokawa, M. Fujiwara and Y. Shimizu, *Soft Matter*, 2009, **5**, 4658–4664.

30   K. Efimenko, J. Finlay, M. E. Callow and J. Genzer, *ACS Appl. Mater. Interfaces*, 2009, **1**, 1031–1040.

31   E. P. Chan, E. J. Smith, R. C. Hayward and A. J. Crosby, *Adv. Mater.*, 2008, **20**, 711–716.

32   C. S. Davis and A. J. Crosby, *Soft Matter*, 2011, **7**, 5373–5381.

33   Y. Li, S. Dai, J. John and K. R. Carter, *ACS Appl. Mater. Interfaces*, 2013, **5**,

11066–11073.

34   C. M. Stafford, C. Harrison, K. L. Beers, A. Karim, E. J. Amis, M. R. VanLandingham, H. C. Kim, W. Volksen, R. D. Miller and E. E. Simonyi, *Nat. Mater.*, 2004, **3**, 545–550.

35   J. Y. Chung, A. J. Nolte and C. M. Stafford, *Adv. Mater.*, 2011, **23**, 349–368.

36   P. J. Yoo, *Electron. Mater. Lett.*, 2011, **7**, 17–23.

37   J. Yin, J. L.Yagüe, D. Eggenspieler, K. K. Gleason and M. C. Boyce, *Adv. Mater.*, 2012, **24**, 5441–5446.

38   N. Bowden, S. Brittain, A. G. Evans, J. W. Hutchinson and G. M. Whitesides, *Nature*, 1998, **393**, 146–149.

39   H. Vandeparre, J. Léopoldès, C. Poulard, S. Desprez, G. Derue, C. Gay and P. Damman, *Phys. Rev. Lett.*, 2007, **99**, 188302.

40   W. Ding, Y. Yang, Y. Zhao, S. Jiang, Y. Cao and C. Lu, *Soft Matter*, 2013, **9**, 3720–3726.

41   G. Miquelard-Garnier, A. B. Croll, C. S. Davis and A. J. Crosbyet, *Soft Matter*, 2010, **6**, 5789–5794.

42   C. J. Rand, R. Sweeney, M. Morrissey, L. Hazel and A. J. Crosbyet, *Soft Matter*, 2008, **4**, 1805–1807.

43   S. J. Yu, Y. J. Zhang, H. Zhou, M. G. Chen, X. F. Zhang, Z. W. Jiao and P. Z. Si, *Phys. Rev. E*, 2013, **88**, 042401.

44   M. D. Huntington, C. J. Engel, A. J. Hryn and T. W. Odom, *ACS Appl. Mater. Interfaces*, 2013, **5**, 6438–6442.

45 M. George, C. Coupeau, J. Colin and J. Grilhé, *Thin solid films*, 2003, **429**, 267–272.

46 J. Jones, S. P. Lacour, S. Wagner and Z. Suo, *J. Vac. Sci. Technol. A*, 2004, **22**, 1723–1725.

47 A. Lucantonio, M. Roché, P. Nardinocchi and H. A. Stone, *Soft Matter*, 2014, **10**, 2800–2804.

48 P. Zhang, D. Yang, Z. Li and H. Ma, *Soft Matter*, 2010, **6**, 4580–4584.

49 J. Huang, M. Juszkiewicz, W. H. de Jeu, E. Cerda, T. Emrick, N. Menon and T. P. Russell, *Science*, 2007, **317**, 650–653.

50 Y. C. Chen and A. J. Crosby, *Adv. Mater.*, 2014, **26**, 5626–5631.

51 S. F. Ahmed, G. H. Rho, K. R. Lee, A. Vaziri and M. W. Moon, *Soft Matter*, 2010, **6**, 5709–5714.

52 P. J. Yoo, K. Y. Suh, S. Y. Park and H. H. Lee, *Adv. Mater.*, 2002, **14**, 1383–1387.

53 F. Xu and Y. Zhu, *Adv. Mater.*, 2012, **24**, 5117–5122.

54 J. Chen, K. E. Wright and M. A. Birch, *Acta Mech. Sin.*, 2014, **30**, 2–6.

55 F. Song and D. Ren, *Langmuir*, 2014, **30**, 10354–10362

Figure captions

Fig. 1 Typical surface morphologies of iron films deposited on completely cured

PDMS substrates with varied film thicknesses taken by the optical microscopy.

The data appearing in the bottom-left corners represent the film thickness. The

average spacing between the neighboring cracks, i.e., the average width of the

closed domains, is denoted as d. Each image has a size of $1390{\times}1040$ μm^2.

The curing time of the PDMS is larger than 3 hours, which is valid for Figs.

1-6.

Fig. 2 Morphological evolution of the homogeneous disordered wrinkles with the

film thickness taken by the Atomic force microscopy (AFM). Each image has

a size of $20{\times}20$ μm^2.

Fig. 3 (a) Typical crack and wrinkle morphologies of the film with the thickness of

90 nm taken by the optical microscopy. The brighter region embedded in the

continuous film is defined as old crack. The darker region accompanied by

parallel straight wrinkles is defined as new crack. The length and period of the

straight wrinkles are denoted as L and λ, respectively. (b) 3-D structural

information of the localized wrinkled stripe taken by the atomic force

microscopy. The image has a size of $40{\times}40$ μm^2. (c) Dependence of the

average crack spacing (i.e., the average domain width) d on the film thickness

h. The solid line is an exponential fit to the experimental data with the

equation shown in the black box. (d) Dependence of the crack width w

(including the old crack and new crack) on the film thickness h.

Fig. 4   (a) Typical surface morphology of the film with the thickness of 225 nm taken by the optical microscopy. (b-d) Enlarged views for the old crack (defined as mode I), the coexistence of old crack and new crack (defined as mode II) and the new crack (or mixed crack) accompanied by localized straight wrinkles (defined as mode III).
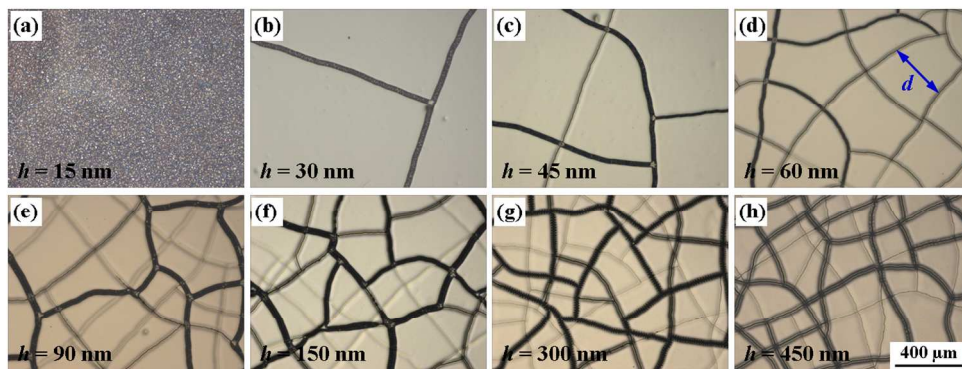
Fig. 5   (a-h) Morphological evolution of the straight wrinkles with increasing the film thickness taken by the atomic force microscopy. The data appearing in the bottom-left corners represent the film thickness. Each AFM image has a size of $40{\times}40$ μm^2. (b) Comparison of the wrinkle profiles for different film thicknesses. Note that the profile lines are shifted artificially along the z-axis for clarity.

Fig. 6   Dependences of the wrinkle length L (a), wrinkle wavelength λ (b), wrinkle amplitude A (c) and their ratio A/λ (d) on the film thickness h. The solid lines in (b) and (c) are linear fits to the experimental data when $h < 300$ nm. The dashed line in (d) is a guide to the eye.
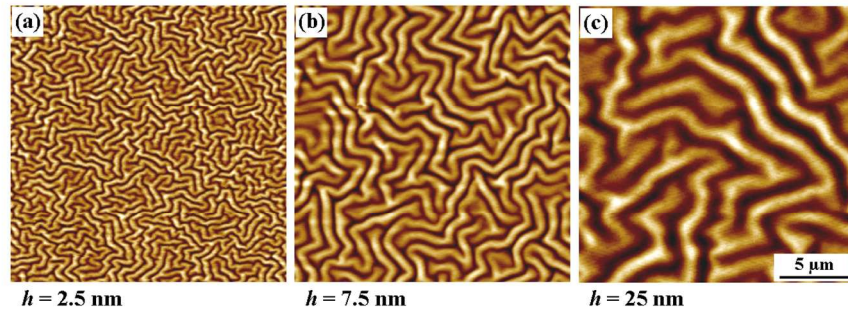
Fig. 7   (a) Typical surface morphologies of the iron films ($h = 90$ nm) deposited on the PDMS substrates with varied curing times taken by the optical microscopy. The data appearing in the bottom-left corners represent the curing time of the PDMS. The dark stripes represent the new cracks accompanied by localized wrinkles and the gray stripes represent the old cracks. Each image has a size of $1390{\times}1040$ μm^2. The film thickness is 90 nm. (b) Morphological evolution of the localized straight wrinkles with increasing the curing time taken by the

27

atomic force microscopy. Each AFM image has a size of 80×80 μm^2. (c)

Comparison of the wrinkle profiles for different curing times. The profile lines

are shifted artificially along the z-axis for clarity. Note that the curing time of

PDMS was changed from 0 to 4 hours in our experiment. It is shown that the

substrate property and wrinkle morphology have no longer changed obviously

when the curing time further increases. Therefore the experimental results for

curing time beyond 20 or 30 minutes are not shown in Figs. 7 and 8.

Fig. 8   Dependences of the average crack spacing d (a), crack width w (b), wrinkle

length L (c), wrinkle wavelength λ (d), wrinkle amplitude A (e) and their

ratio A/λ (f) on the curing time T_c. The solid lines in (a-e) are exponential

fits to the experimental data with the equations shown in the black boxes. The

inset of (c) shows the dependence of the relative wrinkled area L/d on the
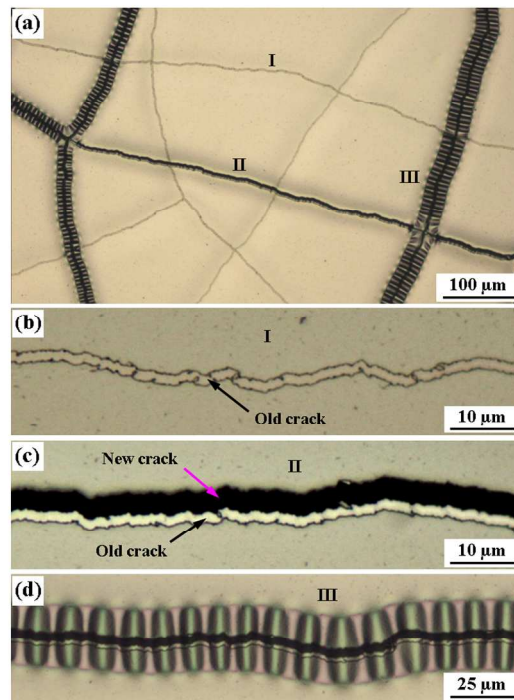
curing time. The dashed line is a guide to the eye.

(a) $h = 15$ nm
(b) $h = 30$ nm
(c) $h = 45$ nm
(d) $h = 60$ nm, d
(e) $h = 90$ nm
(f) $h = 150$ nm
(g) $h = 300$ nm
(h) $h = 450$ nm, 400 μm

254x190mm (150 x 150 DPI)

(a) (b) (c)

5 μm

$h = 2.5$ nm $\qquad$ $h = 7.5$ nm $\qquad$ $h = 25$ nm
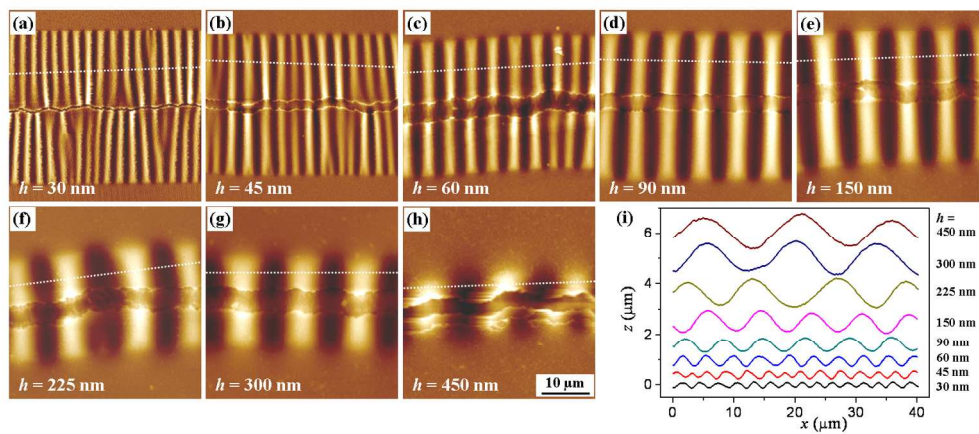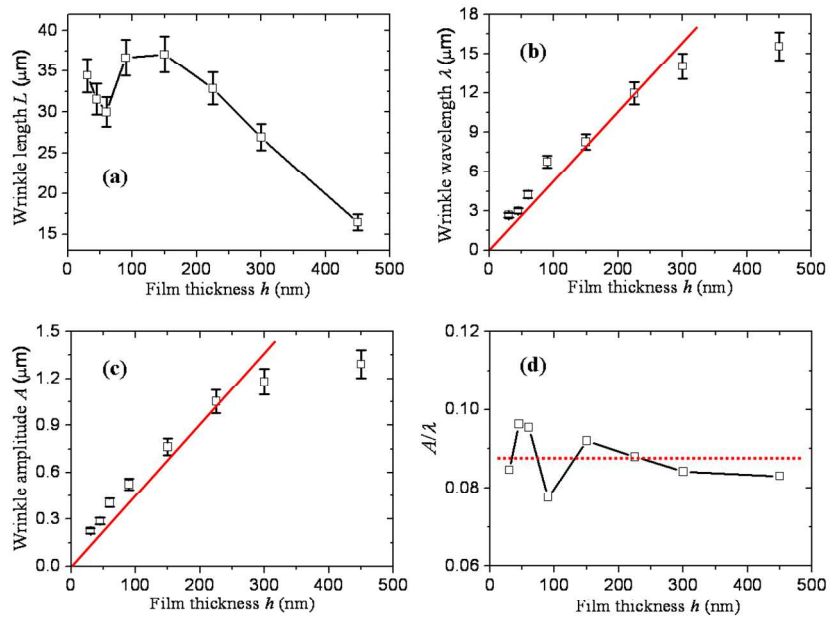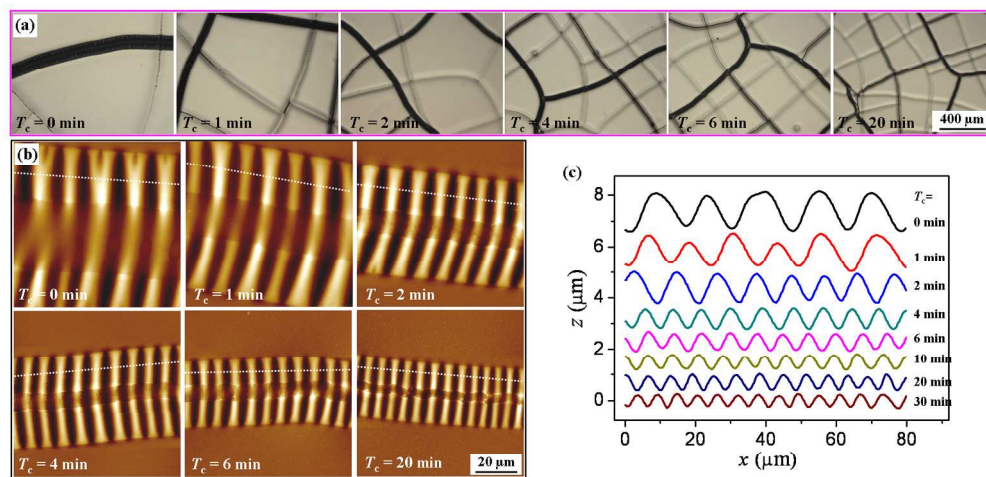
254x190mm (150 x 150 DPI)
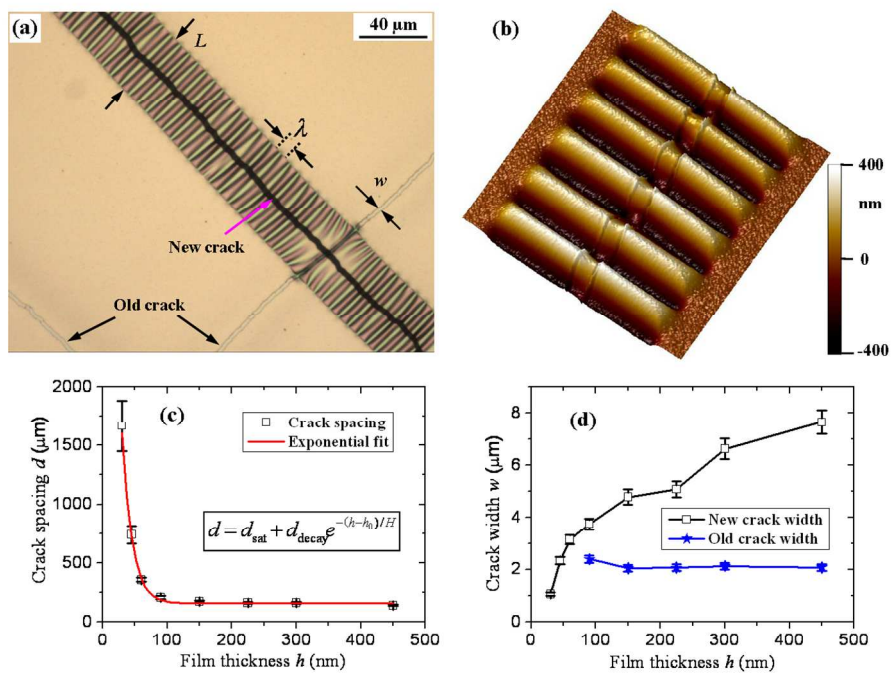
254x190mm (150 x 150 DPI)
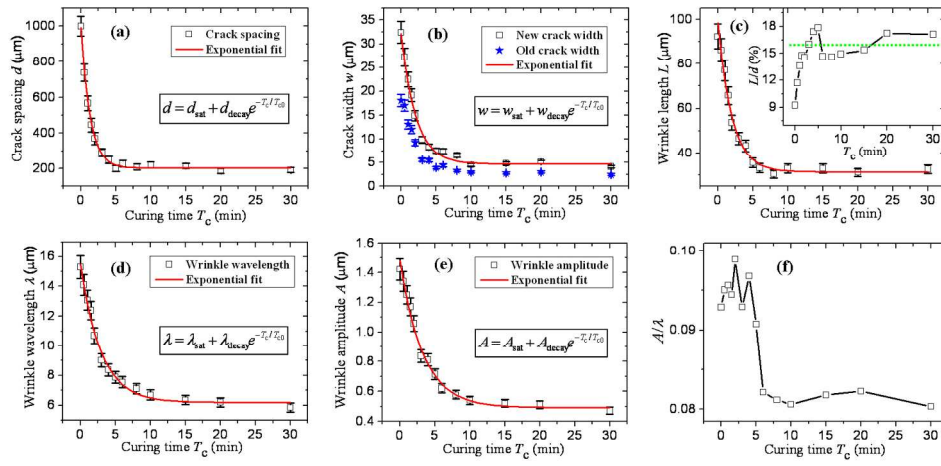
254x190mm (150 x 150 DPI)

311x192mm (150 x 150 DPI)

254x190mm (150 x 150 DPI)

330x190mm (150 x 150 DPI)

334x190mm (150 x 150 DPI)